ACS APPLIED MATERIALS & INTERFACES

www.acsami.org Research Article

Combined Experimental and Computational Insight into the Role of Substrate in the Synthesis of Two-Dimensional WSe_2

Kasra Momeni,* Nuruzzaman Sakib, Daniel E. Cintron Figueroa, Shiddartha Paul, Cindy Y. Chen, Yu-Chuan Lin, and Joshua A. Robinson

Cite This: *ACS Appl. Mater. Interfaces* 2024, 16, 6644−6652 Read Online

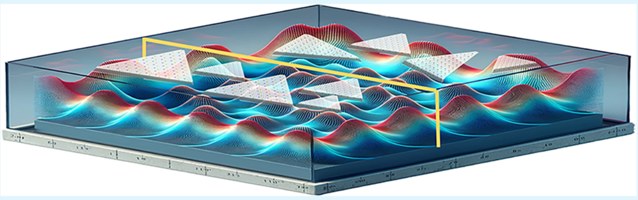

ABSTRACT: Synthesis of large-area transition-metal dichalcogenides (TMDs) with controlled orientation is a significant challenge to their industrial applications. Substrate plays a vital role in determining the final quality of monolayer materials grown via the chemical vapor deposition process by controlling their orientation, crystal structure, and grain boundary. This study determined the binding energy and equilibrium distance for tungsten diselenide (WSe_2) monolayers on crystalline and amorphous silicon dioxide and aluminum dioxide substrates. Differently oriented WSe_2 monolayers are considered to investigate the role of the substrate in the orientation, binding strength, and equilibrium distance. This study can pave the way to synthesizing high-quality two-dimensional (2D) materials for electronic and chemical applications.

KEYWORDS: *reactive molecular dynamics, chemical vapor deposition, tungsten diselenide, 2D materials*

1. INTRODUCTION

In recent years, two-dimensional (2D) materials have attracted significant attention because of their exceptional behaviors and characteristics resulting from atomically thin structures, with promising applications in solar cells[1,2] and flexible electronics.[3,4] Transitional metal dichalcogenides (TMDs) are among the most studied 2D materials since they can be tweaked for unique functionalities. In particular, atomically thin monolayer tungsten diselenide (WSe_2) is of interest because of its tunable electric and optical properties, sizable bandgap, thermo-mechanical stability, and a wide range of applications, including electronics,[5] transistors,[6] gas sensors,[7] photoelectronics,[8] piezolectronics,[9] and light-emitting diodes (LEDs).[10] Leveraging the distinctive characteristics of WSe_2 at an industrial scale necessitates consistent large-area synthesis, underscoring the importance of comprehending the underlying growth mechanisms.[11−13]

Monolayer WSe_2 comprises a layered configuration characterized by a W atom layer sandwiched between two Se atom layers, featuring robust covalent bonds between W and Se layers, with weak van der Waals forces governing the bonding in bulk WSe_2 layers.[14] The synthesis of WSe_2 can be achieved through two primary approaches: mechanical exfoliation, commonly referred to as top-down methods,[15,16] and chemical vapor deposition (CVD) techniques, which fall under the bottom-up synthesis methods.[3,17−19] Mechanically exfoliated WSe_2 has found utility in Na-ion battery applications,[20] transistor fabrication,[21] photon emitters,[22] and gas sensors.[23] Conversely, the CVD process offers a controlled and scalable route for producing defect-free, large-scale 2D materials with specific thickness control, including WSe_2.[3,17−19] This technique involves the formation of solid materials from gaseous precursors, which interact either in the vapor phase or on a substrate's surface. The final structure's layer count, size, and orientation can be precisely tuned by manipulating various process parameters, including substrate type and orientation. A wide array of computational approaches, including finite element analysis,[24−26] atomistic simulation,[27,28] and first-principles method,[29] has been harnessed to provide insights into the synthesis of 2D material.[30−34] While the majority of these investigations primarily center around first-principles/density functional theory (DFT) calculations, their scope remains limited in analyzing larger atomic systems found in TMDs exhibiting specific rotation angles. Consequently, it becomes imperative to employ alternative simulation techniques such as molecular dynamics (MD),[35,36] phase-field,[37,38] or multiscale models[39−42] to gain a comprehensive understanding of the underlying mechanisms governing their growth.

Prior studies have emphasized the significant influence of substrates on the distribution and orientation of 2D materials.[43,44] During the synthesis of 2D materials, substrates play a pivotal role in three fundamental aspects: adsorption of source materials, facilitation of material nucleation, and

Received: November 8, 2023
Revised: January 10, 2024
Accepted: January 11, 2024
Published: January 24, 2024

https://doi.org/10.1021/acsami.3c16761

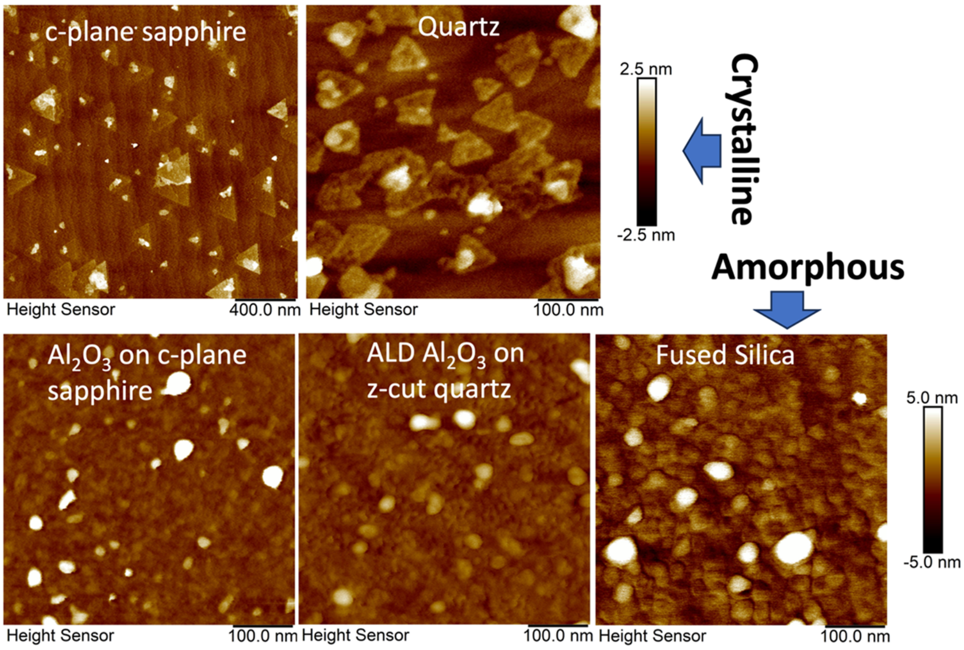

Figure 1. Morphology of as-grown WSe_2 monolayers on crystalline (top row) and amorphous (bottom row) substrates. Epitaxial growth, where the morphology follows the pattern of the substrate, is detected for growth on crystalline substrates. However, only agglomerates of WSe_2 and nonepitaxial growth of WSe_2 on amorphous substrates were detected.

promotion of material epitaxial development.[45,46] This influence extends to the shaping of the island size and orientation, achieved by modifying nucleation processes, precursor species diffusion, and thermodynamic driving forces. The interaction between as-grown 2D materials and the substrate significantly affects the uniformity of monolayer film growth. Several substrate properties, including thermal expansion coefficient, catalytic effects, and lattice mismatch with the desired material, profoundly affect the quality of the resulting 2D materials. Divergence in thermal expansion coefficients leads to inconsistent deformations, ultimately affecting the structural integrity of the deposited material. Catalytic effects, on the other hand, effectively reduce the activation energy, facilitating the necessary reactions.

This investigation delves into the impact of substrates on the orientation of as-grown single-layer WSe_2 monolayers through a comprehensive blend of experimental and theoretical methodologies. The study entails the growth of WSe_2 monolayers on four distinct substrate types, with a focal point on elucidating the atomistic mechanisms responsible for morphological variations in the as-grown monolayers employing reactive molecular dynamics (MD) simulations. Among the substrate materials examined, crystalline and amorphous Al2O3, as well as SiO_2, represent prevalent types. The research is specifically tailored to analyze binding energy, equilibrium distance, and energy landscape attributes of differently oriented WSe_2 monolayers situated on these substrate surfaces. The outcomes of this investigation are expected to lay the groundwork for enhancing the controllability of the CVD process for WSe_2 monolayers, enabling precise orientation control to cater to diverse applications.

2. MATERIALS AND METHODOLOGY

2.1. MOCVD WSe_2 Film Synthesis. WSe_2 growth is achieved in a custom-built Kurt J. Lesker vertical cold wall reactor chamber following the growth model depicted in Figure S1 in the Supporting Information. Four substrate types were considered, i.e., (i) crystalline SiO_2 (*z*-plane quartz), (ii) crystalline Al_2O_3 (*c*-plane sapphire), (iii) amorphous SiO_2, and (iv) amorphous Al_2O_3. The amorphous Al_2O_3 substrate was prepared using the ALD technique by depositing Al_2O_3 on *z*-cut quartz and *c*-plane sapphire. The ALD of Al_2O_3 is performed in a Kurt J. Lesker Company ALD-150LE under a substrate temperature of 200 °C. N_2 gas is used as the process gas to maintain a process pressure of 0.7 Torr. H_2O and $Al_2(CH_3)_6$ precursors are sequentially injected into the chamber at a flow rate of 75 sccm and separated by N_2 purge steps with flow rates of 150 sccm. The ALD cycle consists of: (1) 0.03 s $Al_2(CH_3)_6$ dose, (2) 10 s purge, (3) 0.10 s H_2O dose, and (4) 10 s purge.

To grow WSe_2 on *c*-plane sapphire and *z*-cut quartz, initially, a 10 min anneal is performed at 350 °C to remove any volatile surface-bound species. Afterward, the temperature is increased to 800 °C at a ramp rate of 50 °C/min. Once the temperature reaches 800 °C, both $W(CO)_6$ and H_2Se reactants are introduced to the growth chamber for 10 min at controlled flow rates of 5.1×10^{-3} standard cubic centimeters per minute (sccm) and 78 sccm, respectively. Then, $W(CO)_6$ flow is shut off while hydrogen selenide flow continues at 78 sccm for another 10 min to ensure the removal of any W compound and dangling bonds.[47] Finally, the chamber is cooled at a rate of 30°/min and the H_2Se flow is shut off at 300 °C.

We also grow WSe_2 on the amorphous substrates—i.e., substrates (iii) and (iv)—following a process similar to the growth on crystalline substrates with the exception that the growth and postgrowth anneal temperature is lowered to 600 °C. It has been reported that chalcogen hydride reactants (i.e., H_2S, H_2Se) react with SiO_2 and Al_2O_3 to form ultra-free-standing silica and interfacial AlX_y (X = S, Se) compounds, respectively. Hence, to address safety concerns, the temperature must be kept below 600 °C when using these amorphous substrates.

The WSe_2 domains are on the order of 50−400 nm, making it difficult to observe their morphology with lower-magnification techniques like optical microscopy. Thus, the morphology of the as-grown samples was characterized using atomic force microscopy (AFM). AFM micrographs were acquired using a Bruker Dimension Icon AFM instrument, capturing images at scan sizes of 5 × 5 and 2 × 2 μm^2. The micrographs were obtained employing a ScanAsyst-Air (with a spring constant, k = 0.4 N/m) tip on the same Bruker Dimension Icon apparatus. PeakForce Tapping mode was selected for

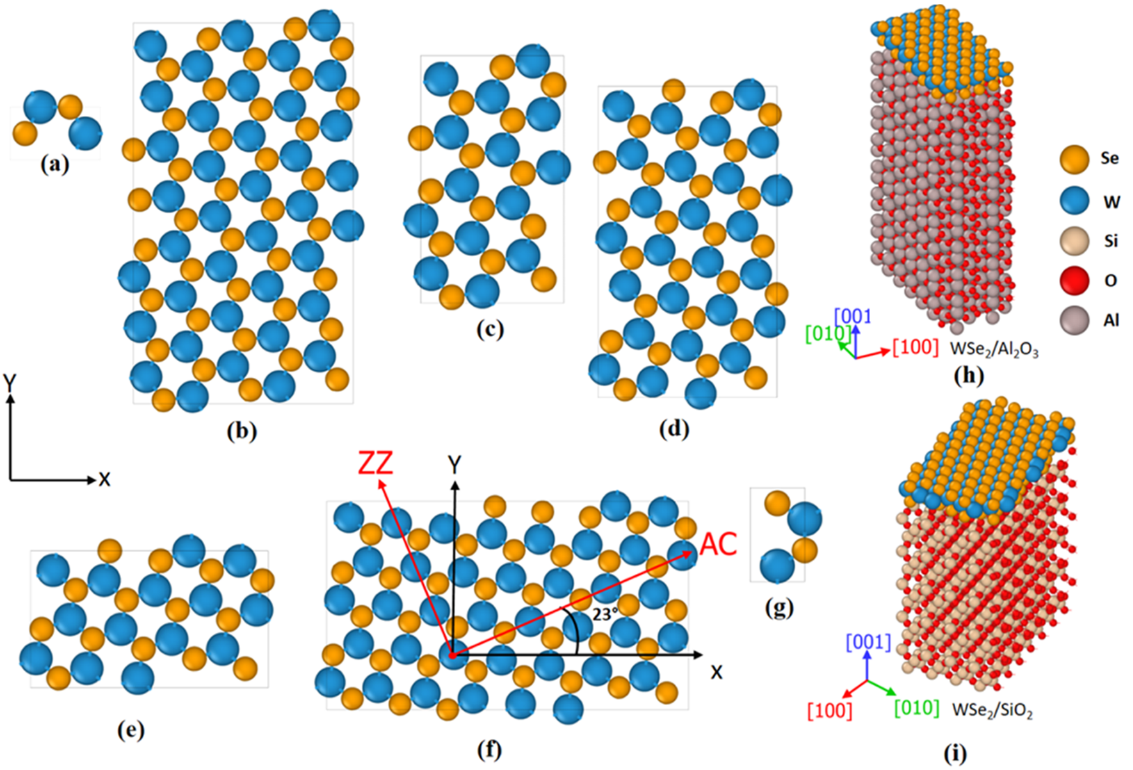

Figure 2. Differently oriented WSe_2 and WSe_2/substrate structures. Unit cells of (a) 0°, (b) 7°, (c) 11°, (d) 14°, (e) 19°, (f) 23°, and (g) 30° rotated WSe_2. Supercells of WSe_2 monolayer on crystalline (h) Al_2O_3 and (i) a SiO_2 substrate.

AFM imaging to ensure optimal image resolution without causing damage to the film. The acquisition parameters were set with a tip scan rate of 0.5 Hz, maintaining a peak force set point of 1.00 nN and a peak force frequency of 2 kHz, ensuring the generation of high-quality micrographs. The images were captured at a resolution of 498 lines per image and a scan rate of 0.9 Hz. The results are shown in Figure 1, while the height analysis is shown in Figures S6 and S7 in the Supporting Information, evidencing a substrate-to-film height of around 0.7 nm,[48] which is the height for monolayer films. Thus, revealing the atomically thin structures of the WSe_2 films grown on crystalline sapphire and quarts.

Our experimental observations reveal the formation of WSe_2 islands with distinct characteristics on various substrates. Specifically, on *c*-plane sapphire and *z*-cut quartz substrates, the WSe_2 islands exhibit a preferred orientation, assuming a triangular morphology (as depicted in Figure 1, top row). In contrast, when grown on amorphous Al_2O_3 substrates, which were deposited using the atomic layer deposition (ALD) technique on both *c*-plane sapphire and *z*-cut quartz, as well as on fused silica substrates, the WSe_2 islands exhibit a random orientation (as illustrated in Figure 1, bottom row).

The triangular shape of the WSe_2 islands on sapphire substrates is characterized by sharp edges, displaying growth orientations of 0 and 60°. Conversely, on quartz substrates, the islands exhibit no discernible orientation preference and feature rounded edges. This disparity in edge geometry can be attributed to differences in the edge-to-surface diffusion ratio of precursor species on quartz and sapphire substrates. Furthermore, the size of WSe_2 islands on quartz substrates is consistently smaller than that on sapphire, indicating potentially slower growth kinetics on quartz. This disparity underscores the influence of substrate material on the growth process.

On amorphous substrates (Figure 1, bottom row), the monolayer WSe_2 islands exhibit a notably high density of small islands. This high density is indicative of a smaller critical nucleus size and a heightened nucleation rate. The slow growth kinetics observed can be associated with the lower growth temperatures enforced on amorphous substrates to avoid the formation of hazardous substances at elevated temperatures. Additionally, the monolayers grown on amorphous substrates lack a preferred growth morphology, as these substrates lack a defined crystalline direction. The higher surface roughness of amorphous substrates may contribute to reduced interactions between the as-grown film and the substrate.

2.2. Computational Model.

The experimental findings presented in this study reveal the substantial influence of substrate characteristics on the distribution and orientation of the WSe_2 triangular islands, as illustrated in Figure 1. On quartz substrates, the synthesized WSe_2 triangular islands exhibit arbitrary orientations, whereas those grown on sapphire substrates display a preference for 0° orientations. The uniform orientation distribution of these islands is intricately linked to the interplay between the as-grown 2D materials and the substrate. This dynamic interaction plays a pivotal role in shaping the islands in terms of their size and orientation, exerting influence over the nucleation process and growth-driving forces. To further understand the atomistic mechanisms governing the growth of WSe_2 monolayers on different substrates, we used reactive MD simulations.

Our investigation delves into the influence of in-plane orientation angles of atomically thin WSe_2 structures in relation to the substrate's normal, focusing on the variations in binding energy and equilibrium distance. To comprehensively assess this effect, we have employed four distinct substrate materials, namely, crystalline and amorphous Al_2O_3 and SiO_2 substrates.

The procedure entails the creation of unit cells for WSe_2, each possessing different in-plane rotation angles with respect to the substrate. Specifically, we considered rotation angles for WSe_2 were 0, 7, 11, 14, 19, 23, and 30° (Figure 2). The selection of these orientation angles aligns with the intrinsic 3-fold rotational symmetry exhibited by 2D WSe_2, ensuring that structures within the 0−30° range are representative, while also acknowledging that structures at 60°- θ angles represent mirrored counterparts.

Taking the unit cell dimension of rotated WSe_2 and the substrate as ($\boldsymbol{a}_{rot}$,$\boldsymbol{b}_{rot}$) and ($\boldsymbol{a}_{sub}$,$\boldsymbol{b}_{sub}$), respectively, the lattice mismatch decreases as $|n_{rot}.\boldsymbol{a}_{rot} - n_{sub}.\boldsymbol{a}_{sub}|$ and $|m_{rot}.\boldsymbol{b}_{rot} - m_{sub}.\boldsymbol{b}_{sub}|$ approaches zero, where n_{rot}, n_{sub}, m_{rot}, and m_{sub} are integers that represent the number of replications of the unit cell in the supercell, determining the size of the simulation cell. Figure 3 represents the lattice mismatch for 11° rotated monolayer WSe_2 on crystalline Al_2O_3 with the number of unit cells in planar directions ([100] and [010]). To maintain minimal misfit strain between the substrate and the as-grown 2D material, the orientation angle limits the unit cell's size (additional details are available in the Supporting Information). These specific orientation angles were chosen to ensure the computational feasibility of the simulation cell sizes. Subsequently, a supercell with minimal lattice mismatch was created for each of the rotated WSe_2-substrate cell configurations. The unit cell dimensions of 0° oriented WSe_2 and substrates are shown in Table S1 in the Supporting Information. The dimensions of rotated WSe_2 structures (Table S2) and the final supercell of the WSe_2/Al_2O_3 (Table S3) and WSe_2/SiO_2 (Table S4) system are provided in the Supporting Information. In order to eliminate the minor lattice mismatch between the WSe_2 supercell and the substrate supercell, the WSe_2 supercells were subjected to the necessary strain.

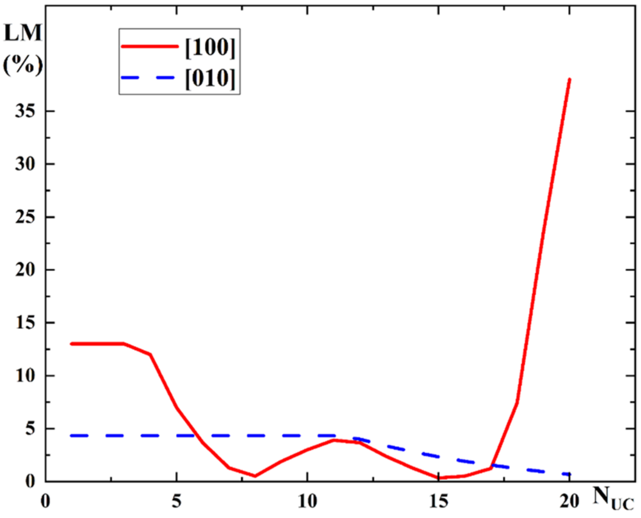

Figure 3. Lattice mismatch percentage (LM) vs number of unit cells (N_{UC}) for 11 oriented monolayer WSe_2 and Al_2O_3 substrate. The number of unit cells in the supercell is chosen by considering the minimum lattice mismatch and size of the supercell. The remaining lattice mismatch present in the supercell is removed by straining the monolayer WSe_2 supercell.

All MD simulations were conducted using the open-source Large-scale Atomic/Molecular Massively Parallel Simulator (LAMMPS) software package.[49] A uniform time step of 0.25 fs was employed for all simulations. In the simulations, periodic boundary conditions were applied in the planar directions (x and y), while a nonperiodic boundary condition was implemented in the out-of-plane direction to prevent interference with the mirrored structure. To capture the interactions within the system, we utilized the ReaxFF force field[50] to model WSe_2[51] and Al_2O_3,[52] while the Tersoff potential[53] was applied for modeling SiO_2. The interactions between WSe_2 and the substrates were described using the Lennard-Jones (LJ) potential, with specific parameters provided in Table S5. For comprehensive details regarding structure preparation and an in-depth discussion of the force field, refer to the Supporting Information.

2.2.1. Preparation of Amorphous SiO_2 Substrate. Amorphous SiO_2 samples were made by randomly introducing silicon and oxygen atoms in a stoichiometric ratio in a simulation box. The dimensions of the simulation box were tailored to match those of the WSe_2 structure. The total number of SiO_2 atoms was determined under the assumption that the amorphous structure possessed the same density as a crystal structure of an equivalent size. Initially, geometric optimization of the simulation cell was conducted, utilizing the conjugate gradient method to alleviate atom overlapping. Subsequently, the cell was subjected to heating, reaching 8000 K within an NVT ensemble and maintained at this temperature for 1 ns.

Then, the reaction was quenched to 300 K at a cooling rate of 10^{11} K/s. A similar cooling rate[46,54] has been used in many studies to create amorphous silica. Following quenching, the structure underwent relaxation under NPT conditions at 300 K and atmospheric pressure for 0.1 ns. Temperature and pressure damping coefficients were set at 100 and 5000 fs, respectively. The resulting structure exhibited a density of approximately ~2.145 g/cm^3. Ten distinct samples were generated by varying the initial velocities within the simulation, each converging to a final structure with a density of ~2.145 g/cm^3.

2.2.2. Preparation of Amorphous Al_2O_3 Substrate. A method similar to that for creating amorphous SiO_2 is utilized to generate the amorphous Al_2O_3 structures. Initially, a simulation box was constructed mirroring the process for amorphous SiO_2. Subsequently, the structure underwent geometric minimization through a conjugate gradient algorithm to mitigate atom overlapping. Later, the structure was heated to 5000 K using an NVT ensemble for 5 ps. This was succeeded by a cooling phase, during which the temperature decreased to 3000 K at a cooling rate of 3.3×10^{14} K/s, and the structure relaxed at this temperature for 5.5 ps. Finally, the substrate underwent a final cooling phase, reaching 300 K at a cooling rate of 3.6×10^{13} K/s, with relaxation occurring at that temperature under atmospheric pressure using an NPT ensemble. Temperature and pressure damping coefficients were set at 100 and 5000 fs, respectively. This approach closely resembled a previously applied method for the creation of amorphous.[55] Ten separate samples were generated by employing different initial seed velocities, resulting in final structures with a density of approximately 3.4 g/cm^3.

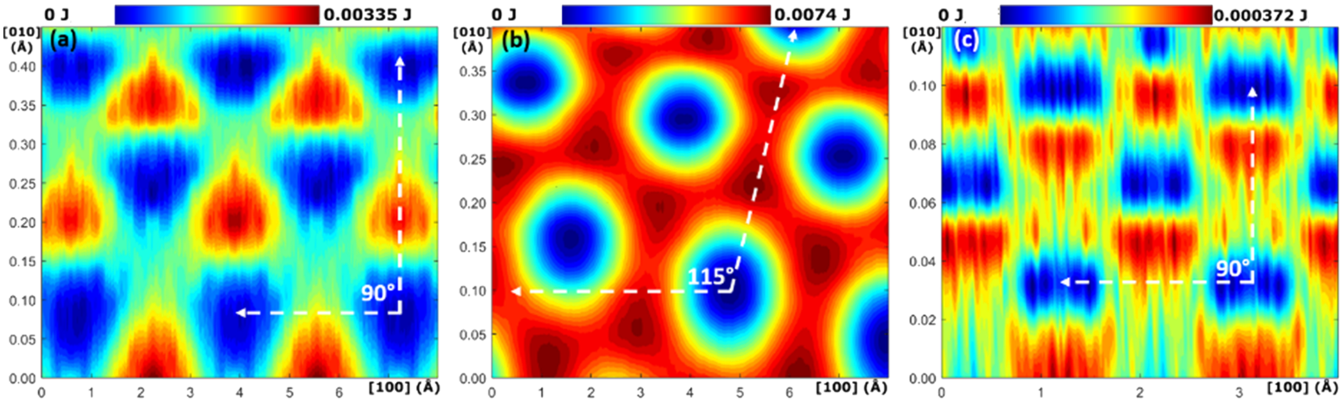

Figure 4. Energy landscape for differently oriented WSe_2/Al_2O_3: (a) 0°, (b) 14°, and (c) 30° rotated WSe_2. The color bar represents energy (J). Minimum energy is considered 0.

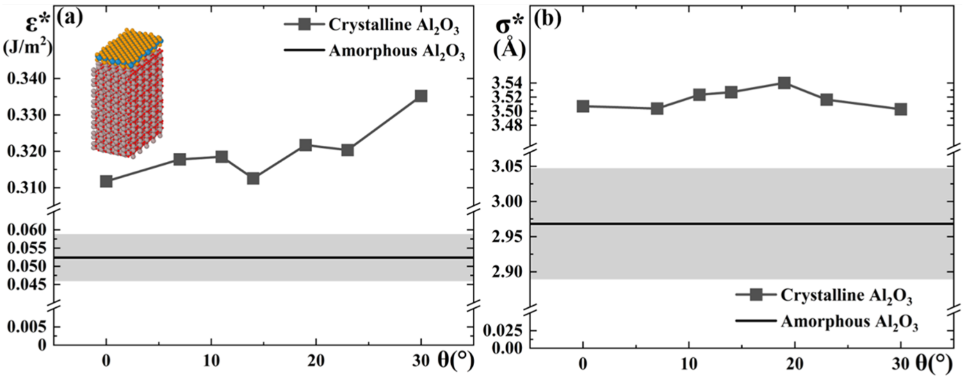

Figure 5. Interaction between differently oriented WSe_2 and Al_2O_3 substrate: (a) binding energy, ε^* (J/m^2) and (b) equilibrium distance, σ^* (Å) vs rotation angle, θ (deg) of 2D WSe_2. The shaded area represents errors. For amorphous substrates, a singular WSe_2 structural configuration was analyzed in conjunction with 10 distinct substrate variations, given that orientation angles are indeterminate for amorphous materials. The shaded region depicted within the graphical representation corresponds to the error margin attributed to the inclusion of various amorphous structures.

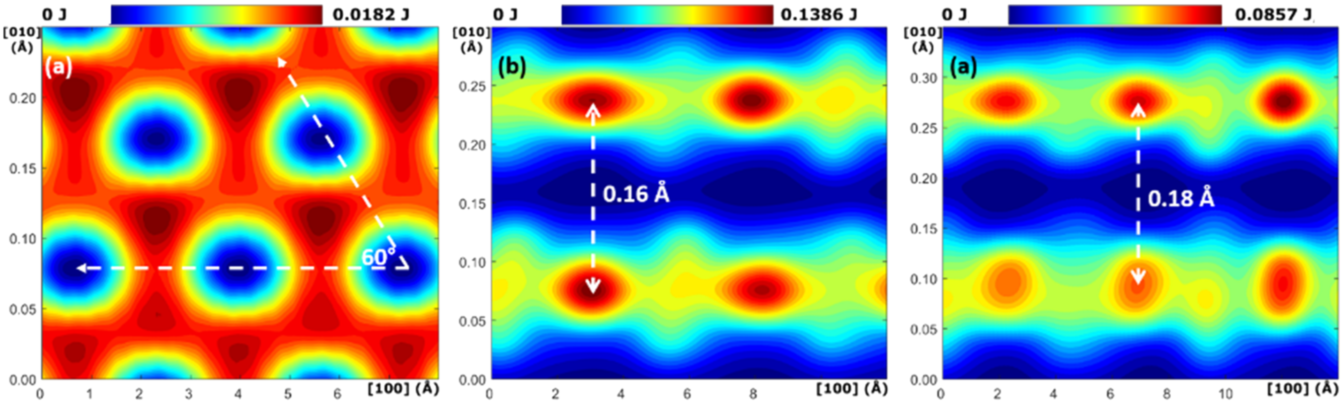

Figure 6. Energy surface for differently oriented WSe_2/SiO_2: (a) 0°, (b) 14°, and (c) 30° rotated WSe_2. The color bar represents the energy (*J*). Minimum energy is considered zero.

2.2.3. Binding Energy and Energy Landscape of WSe_2 on Different Substrates. We conducted a comprehensive assessment of the binding energy and energy landscape associated with monolayer WSe_2 interfacing with a variety of substrates. To facilitate this analysis, we positioned the WSe_2 monolayers at a vertical distance beyond the predefined cutoff radius for van der Waals interactions, which adheres to the parameters set by the Lennard-Jones potential, specifically, 10.5 Å.

The process of obtaining the equilibrium structure encompasses several distinct phases. Initially, we employed a conjugate gradient algorithm to minimize the entire structural configuration. Subsequently, the structure underwent relaxation at a temperature of 1 K, using the NVE ensemble, with velocity rescaling applied to the thermostat. This was followed by a subsequent relaxation step at 1 K and atmospheric pressure under the NPT ensemble. It is worth noting that our choice of parameters included a temperature-damping coefficient of 100 fs and a pressure damping coefficient of 5000 fs.

The determination of binding energy and equilibrium distance, pertaining to the interaction between the monolayer WSe_2 and the substrates, was carried out by gradually displacing the WSe_2 monolayer toward the substrate at a constant speed of 2.5 Å/fs. The binding energy values for differently oriented WSe_2 structures on quartz and sapphire substrates can be found in Figures S2 and S3 in the Supporting Information.

To construct the energy landscape, we initiated the process by situating WSe_2 monolayers at their equilibrium distance from the substrate. Subsequently, we systematically conducted a parallel scan of the WSe_2 monolayer along the substrate's surface. This scanning procedure was executed by displacing the WSe_2 monolayer initially by 1/20 of the W−W bond length in the *b*-crystallographic direction ([010]). Subsequent steps involved sequential movements of 1/20 of the W−Se bond length in the a-crystallographic direction ([100]). These incremental steps facilitated the detailed capture of intricate interactions occurring along each bond.

3. RESULTS AND DISCUSSION

Figure 4 illustrates the energy landscape concerning three distinct orientations of WSe_2 monolayers on a crystalline Al_2O_3 (sapphire) substrate. The energy well and peak regions, represented by alternating blue and red segments, portray an eggshell potential energy landscape. Notably, this distinctive energy landscape pattern is consistent across all orientations of WSe_2 on sapphire, as demonstrated in Figure S4.

This type of energy landscape effectively confines the WSe_2 nuclei formed on the substrate, thus promoting a favored growth orientation. Consequently, it suggests the feasibility of nucleation and growth of WSe_2 islands with varying orientations. Among the various orientations examined, the saddle point between adjacent minima is smallest for a 0° misorientation angle between the WSe_2 structures. This observation indicates a higher likelihood of coalescence among nuclei formed with a 0° misorientation angle. This finding aligns with the experimental results presented in Figure 1, which illustrate the growth of WSe_2 monolayers characterized by preferential 0 and 180° orientations.

Figure 5 presents the binding energy and equilibrium distance characteristics of WSe_2 monolayers on both crystalline and amorphous Al_2O_3 substrates. The lowest binding energy is evident when the WSe_2 monolayer is oriented at 0°, followed

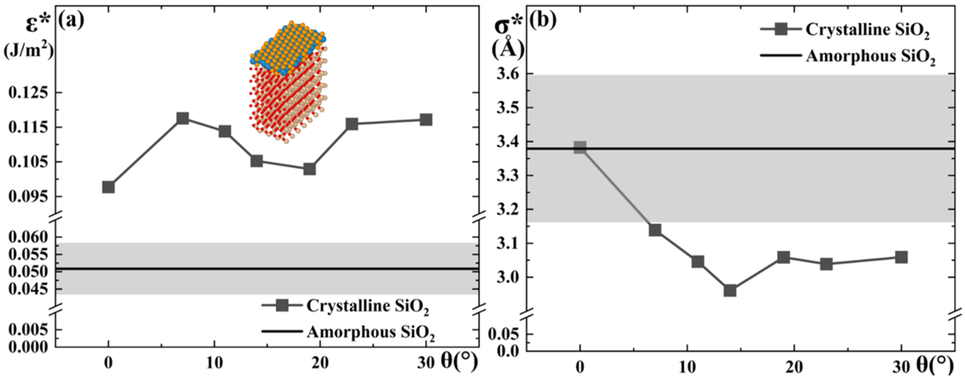

Figure 7. Interaction between differently oriented WSe_2 and crystalline/amorphous SiO_2 substrates. (a) Binding energy, ε^* (J/m^2) and (b) equilibrium distance, σ^* (Å) vs rotation angle, θ (deg) of 2D WSe_2. For amorphous substrates, a singular WSe_2 structural configuration was analyzed in conjunction with 10 distinct substrate variations, given that orientation angles are indeterminate for amorphous materials. The shaded region depicted within the graphical representation corresponds to the error margin attributed to the inclusion of various amorphous structures.

by a gradual increase in binding energy as the orientation angle progresses up to 11°. Subsequently, the 14° orientation exhibits the second-lowest binding energy, with a subsequent gradual increase before reaching the maximum binding energy at a 30° orientation. Exact analytical analysis is not feasible considering the complexity of the combined WSe_2/Al_2O_3 structure and mismatch strains. However, the presence of this local minimum could be because both WSe_2 and sapphire have hexagonal symmetries, with a rotational symmetry angle of $\theta = 60°$, where $14° \approx \theta/4$. In terms of equilibrium distance, the highest value is observed at a 19° rotation angle, whereas the lowest equilibrium distances are associated with orientations at 0, 7, and 30°, with 30° representing the minimum. Notably, there is an increasing trend in equilibrium distance from 7 to 19°, followed by a decreasing trend from 19 to 30°.

The binding energy and equilibrium distance observed for the WSe_2 monolayer on an amorphous Al_2O_3 substrate (Table S6) are measured at 0.052 ± 0.0065 J/m^2 and 2.968 ± 0.079 Å, respectively. These values are smaller than the crystalline system (Figure 5), a phenomenon that can be attributed to the absence of a well-defined crystalline structure in the substrates. This condition of low binding energy, coupled with the lack of crystalline structure, promotes the growth of polycrystalline monolayer WSe_2. Additionally, the lower binding energy facilitates the effortless detachment of the grown WSe_2 from the substrate, offering potential advantages for practical applications.[56,57]

For the crystalline SiO_2 (quartz) substrate, as illustrated in Figures 6 and S5, the energy landscape exhibits a stark contrast compared with that observed on a sapphire substrate. Specifically, the eggshell potential phenomenon manifests exclusively in the case of 0° rotated WSe_2 configurations, where energy minima are distinctly separated by formidable energy barriers, effectively impeding the coalescence of nuclei formed by 0°-oriented WSe_2. In contrast, the energy landscape for rotated WSe_2 structures portrays a striped energy profile, indicating the absence of energy barriers along the stripes for atomic coalescence and a minor energy barrier for the merging of different stripes on the substrate. Consequently, variously oriented WSe_2 monolayers can materialize on the quartz substrate, aligning with the experimental findings presented in Figure 1. Specifically, the lowest and highest energy barriers are encountered for 11 and 19° oriented WSe_2 on the quartz substrate, respectively.

The binding energy and equilibrium distance for WSe_2 on crystalline and amorphous SiO_2 are shown in Figure 7. The binding energy exhibits extrema at 0 and 7° orientations of WSe_2, with a gradual decrease from 7° to a secondary minimum at 19°, followed by a gradual increase up to the 30° orientation. Regarding equilibrium distance, the highest value occurs at 0° orientation, while lower values are observed at 14° orientation. The configurations at 19, 23, and 30° orientations fall between the minimum and maximum values.

The binding energy and equilibrium distance of WSe_2/amorphous SiO_2 (Table S7) are 0.051 ± 0.008 J/m^2 and 3.379 ± 0.218 Å, respectively. In a manner similar to the behavior observed on amorphous Al_2O_3 substrates, the binding energy of WSe_2 with a fused silica substrate is found to be lower than that with a quartz substrate. However, it is noteworthy that the equilibrium distance between WSe_2 and fused silica exceeds that with quartz, and this difference is reduced with an increase in the misorientation angle. The equilibrium distance plays a pivotal role in the selection of suitable intercalating species, with significant implications for the choice of exfoliating agents, functionalizing agents, and confinement heteroepitaxy strategies.[58] Hence, the judicious selection of the substrate is instrumental in facilitating seamless postgrowth processes, thereby directly influencing the quality of the final synthesized material and the performance of the resulting devices.

The binding energy and equilibrium distance in relation to various rotation angles, as depicted in Figures 5 and 7, are calculated by matching the unit cell size of the rotated WSe_2 to the underlying substrate while minimizing strain due to mismatch. Unlike simple biatomic systems where higher binding energy usually corresponds to a smaller equilibrium distance, the complex structure of the supercell and the presence of different elastic energies stemming from distinct mismatch strains make it challenging to establish a direct correlation between binding energy and equilibrium distance across different rotation angles.

The melting temperatures of quartz and sapphire are 1820 and 2044 °C, respectively, significantly higher than the growth temperature of 800 °C. As a result, the influence of temperature on the substrate's structure and energy landscape is deemed negligible. At the specified growth temperature of 800 °C, the thermal energy (k_BT) equates to 1.48×10^{-20} J. The binding energies between WSe_2 and sapphire and quartz substrates measure approximately 0.3 and 0.1 J/m^2, respectively. By considering the dimensions of differently oriented

WSe_2 unit cells on these substrates, as outlined in Tables S3 and S4, it becomes evident that the WSe_2−Al_2O_3/SiO_2 debonding energy exceeds the thermal energy at the growth temperature by an order of magnitude. Consequently, the impact of the growth temperature on the orientation of the resulting WSe_2 monolayers is deemed negligible if the initial WSe_2 nucleus has the same size as the WSe_2−Al_2O_3/SiO_2 unit cells.

In contrast, if the initial WSe_2 nucleus forming on the substrate were equivalent to a single standalone WSe_2 unit cell, which has an area of 13.2 $Å^2$, the debonding energies associated with Al_2O_3 and SiO_2 substrates would be approximately 3.96×10^{-20} and 1.32×10^{-20} J, respectively. In such a scenario, while thermal fluctuations would not significantly affect the growth orientation of WSe_2 on sapphire, they could lead to debonding of the WSe_2 unit cell grown on a quartz substrate. This, in turn, would result in growth with arbitrary orientations, aligning with our experimental observations.

4. CONCLUSIONS

The comprehensive set of results presented in this study enhances our insights into the growth mechanisms governing the synthesis of 2D materials. Specifically, it sheds light on the critical role of the substrate in influencing the quality and uniformity of monolayer films, which are of paramount importance for large-scale industrial applications spanning various sectors, including electronics and defense. Our experimental findings corroborate the computational predictions, notably the preferential growth orientation of WSe_2 monolayers on sapphire substrates compared to the lack of orientation preference on quartz substrates. This behavior is attributed to the distinct energy landscapes of differently oriented WSe_2 monolayers and the potential debonding events driven by thermal energy during growth.

Notably, our findings underscore the profound influence of the substrate structure on the growth orientation of WSe_2 monolayers. Specifically, we observed that sapphire substrates facilitate the formation of 0° rotated WSe_2 monolayers, enabling the synthesis of highly uniform monolayer films. This effect is attributed to the presence of eggshell surface potential with a minimal energy barrier at the saddle point for the 0° misorientation angle between WSe_2 and sapphire, facilitating the coalescence of nuclei and the formation of large-area WSe_2 monolayers with a preferred growth orientation. Furthermore, our investigations revealed the existence of a striped energy landscape between quartz and WSe_2 monolayers for all rotation angles between the substrate and monolayers except for the 0° misorientation. This energy landscape implies a seamless coalescence of WSe_2 nuclei along the stripes, suggesting the absence of a distinct preferred growth orientation for WSe_2 grown on quartz, as corroborated by our experimental findings.

Our investigation reveals that WSe_2 exhibits a higher binding energy when interfacing with crystalline substrates compared to that of amorphous substrates, encompassing both SiO_2 and Al_2O_3 substrates. This observation suggests that WSe_2 growth on amorphous substrates may offer enhanced transferability. However, it is noteworthy that the absence of any distinct energy landscape features between WSe_2 and amorphous substrates implies the formation of a polycrystalline morphology, aligning with our experimental findings. Here, we have considered perfect crystalline WSe_2 and plan to consider the role of defects[59] in our future studies.

Furthermore, our results elucidate a reduction in the spacing between the Al_2O_3 substrates and WSe_2 monolayers following amorphization. In contrast, such amorphization leads to an increase in spacing for quartz substrates. These findings carry significant implications for the selection of substrates in postsynthesis processes, including functionalization, transfer, and device fabrication. The results carry implications for controlling the substrate's placement relative to the flow direction. In scenarios characterized by varied energy landscapes, islands with energy gradients perpendicular to the growth orientation are more likely to thrive. This hypothesis can be validated by examining island morphology on substrates cut along diverse crystalline planes and positioned at the same angle with respect to the flow direction, such as in horizontal CVD furnaces. Alternatively, substrates cut along the same crystalline direction but oriented differently with respect to the flow direction, as seen in vertical CVD growth chambers, can provide equivalent insights.

Additionally, our findings underscore the influence of the growth temperature on island orientation. Higher temperatures can supply sufficient thermal energy to disrupt bonds between the initial monolayer nucleus and the substrate, thereby encouraging growth along alternative orientations. However, it is crucial to note that the temperature exerts a multifaceted impact on monolayer growth. It affects the critical nucleus size, which, in turn, impacts the binding energy with the substrate due to variations in the bonded area. Simultaneously, an elevated thermal energy promotes debonding. Consequently, rigorous experimental investigations are necessary to execute growth at temperatures approximating the debonding energy between monolayers and the substrate. Temperature variations also influence precursor diffusion and nucleation rates, necessitating adjustments to growth conditions.

■ ASSOCIATED CONTENT

Supporting Information

The Supporting Information is available free of charge at https://pubs.acs.org/doi/10.1021/acsami.3c16761.

Additional experimental and simulation details, including photographs of experimental measurements, atomistic structure, and additional calculation results (PDF)

■ AUTHOR INFORMATION

Corresponding Author

Kasra Momeni − *Department of Mechanical Engineering, The University of Alabama, Tuscaloosa, Alabama 35487, United States;* orcid.org/0000-0002-4209-1129; Email: kmomeni@ua.edu

Authors

Nuruzzaman Sakib − *Department of Mechanical Engineering, The University of Alabama, Tuscaloosa, Alabama 35487, United States;* orcid.org/0000-0002-1764-2048

Daniel E. Cintron Figueroa − *Department of Chemistry, The Pennsylvania State University, University Park, Pennsylvania 16802, United States*

Shiddartha Paul − *Department of Mechanical Engineering, The University of Alabama, Tuscaloosa, Alabama 35487, United States; Department of Mechanical Engineering, The University of Illinois at Urbana−Champaign, Urbana,* *Illinois 61801, United States;* orcid.org/0000-0003-4306-180X

Cindy Y. Chen − *Department of Materials Science and Engineering, The Pennsylvania State University, University Park, Pennsylvania 16802, United States*

Yu-Chuan Lin − *Department of Materials Science and Engineering, National Yang Ming Chiao Tung University, Hsin-Chu 30010, Taiwan*

Joshua A. Robinson − *Department of Materials Science and Engineering, The Pennsylvania State University, University Park, Pennsylvania 16802, United States;* orcid.org/0000-0002-1513-7187

Complete contact information is available at:
https://pubs.acs.org/10.1021/acsami.3c16761

Notes

The authors declare no competing financial interest.

ACKNOWLEDGMENTS

This project was partly supported by the National Science Foundation 2D Crystal Consortium−Material Innovation Platform (2DCC-MIP) under NSF cooperative agreement DMR-1539916 and the NSF-CAREER under NSF cooperative agreement CBET-2042683. The authors thank Akash for his assistance.

REFERENCES

(1) Prasad, G.; Srivastava, O. N. The High-Efficiency (17.1%) WSe $_2$ Photo-Electrochemical Solar Cell. *J. Phys. D: Appl. Phys.* **1988**, *21* (6), 1028−1030.

(2) Kakavelakis, G.; Del Rio Castillo, A. E.; Pellegrini, V.; Ansaldo, A.; Tzourmpakis, P.; Brescia, R.; Prato, M.; Stratakis, E.; Kymakis, E.; Bonaccorso, F. Size-Tuning of WSe$_2$ Flakes for High Efficiency Inverted Organic Solar Cells. *ACS Nano* **2017**, *11* (4), 3517−3531.

(3) Huang, J.-K.; Pu, J.; Hsu, C.-L.; Chiu, M.-H.; Juang, Z.-Y.; Chang, Y.-H.; Chang, W.-H.; Iwasa, Y.; Takenobu, T.; Li, L.-J. Large-Area Synthesis of Highly Crystalline WSe $_2$ Monolayers and Device Applications. *ACS Nano* **2014**, *8* (1), 923−930.

(4) Cheng, Q.; Pang, J.; Sun, D.; Wang, J.; Zhang, S.; Liu, F.; Chen, Y.; Yang, R.; Liang, N.; Lu, X.; Ji, Y.; Wang, J.; Zhang, C.; Sang, Y.; Liu, H.; Zhou, W. WSe$_2$ 2D P-type Semiconductor-based Electronic Devices for Information Technology: Design, Preparation, and Applications. *InfoMat* **2020**, *2* (4), 656−697.

(5) Doan, M.-H.; Jin, Y.; Chau, T. K.; Joo, M.-K.; Lee, Y. H. Room-Temperature Mesoscopic Fluctuations and Coulomb Drag in Multilayer WSe2. *Adv. Mater.* **2019**, *31* (17), No. 1900154.

(6) Pudasaini, P. R.; Stanford, M. G.; Oyedele, A.; Wong, A. T.; Hoffman, A. N.; Briggs, D. P.; Xiao, K.; Mandrus, D. G.; Ward, T. Z.; Rack, P. D. High Performance Top-Gated Multilayer WSe2 Field Effect Transistors. *Nanotechnology* **2017**, *28* (47), No. 475202.

(7) Chen, Y.-Z.; Lee, S.-H.; Su, T.-Y.; Wu, S.-C.; Chen, P.-J.; Chueh, Y.-L. Phase-Modulated 3D-Hierarchical 1T/2H WSe2 Nanoscrews by a Plasma-Assisted Selenization Process as High Performance NO Gas Sensors with a Ppb-Level Detection Limit. *J. Mater. Chem. A* **2019**, *7* (39), 22314−22322.

(8) Patel, A. B.; Machhi, H. K.; Chauhan, P.; Narayan, S.; Dixit, V.; Soni, S. S.; Jha, P. K.; Solanki, G. K.; Patel, K. D.; Pathak, V. M. Electrophoretically Deposited MoSe2/WSe2 Heterojunction from Ultrasonically Exfoliated Nanocrystals for Enhanced Electrochemical Photoresponse. *ACS Appl. Mater. Interfaces* **2019**, *11* (4), 4093−4102.

(9) Zhu, H.; Wang, Y.; Xiao, J.; Liu, M.; Xiong, S.; Wong, Z. J.; Ye, Z.; Ye, Y.; Yin, X.; Zhang, X. Observation of Piezoelectricity in Free-Standing Monolayer MoS2. *Nat. Nanotechnol.* **2015**, *10* (2), 151−155.

(10) Yu, L.; Zubair, A.; Santos, E. J. G.; Zhang, X.; Lin, Y.; Zhang, Y.; Palacios, T. High-Performance WSe2 Complementary Metal Oxide Semiconductor Technology and Integrated Circuits. *Nano Lett.* **2015**, *15* (8), 4928−4934.

(11) Momeni, K.; Ji, Y.; Chen, L.-Q. Computational Synthesis of 2D Materials Grown by Chemical Vapor Deposition. *J. Mater. Res.* **2022**, *37* (1), 114−123.

(12) Paul, S.; Torsi, R.; Robinson, J. A.; Momeni, K. Effect of the Substrate on MoS$_2$ Monolayer Morphology: An Integrated Computational and Experimental Study. *ACS Appl. Mater. Interfaces* **2022**, *14* (16), 18835−18844.

(13) Momeni, K.; Ji, Y.; Zhang, K.; Robinson, J. A.; Chen, L.-Q. Multiscale Framework for Simulation-Guided Growth of 2D Materials. *npj 2D Mater. Appl.* **2018**, *2* (1), No. 27.

(14) Johari, P.; Shenoy, V. B. Tuning the Electronic Properties of Semiconducting Transition Metal Dichalcogenides by Applying Mechanical Strains. *ACS Nano* **2012**, *6* (6), 5449−5456.

(15) Fang, H.; Chuang, S.; Chang, T. C.; Takei, K.; Takahashi, T.; Javey, A. High-Performance Single Layered WSe2 p-FETs with Chemically Doped Contacts. *Nano Lett.* **2012**, *12* (7), 3788−3792.

(16) Ross, J. S.; Klement, P.; Jones, A. M.; Ghimire, N. J.; Yan, J.; Mandrus, D. G.; Taniguchi, T.; Watanabe, K.; Kitamura, K.; Yao, W.; Cobden, D. H.; Xu, X. Electrically Tunable Excitonic Light-Emitting Diodes Based on Monolayer WSe2 p-n Junctions. *Nat. Nanotechnol.* **2014**, *9* (4), 268−272.

(17) Zhou, H.; Wang, C.; Shaw, J. C.; Cheng, R.; Chen, Y.; Huang, X.; Liu, Y.; Weiss, N. O.; Lin, Z.; Huang, Y.; Duan, X. Large Area Growth and Electrical Properties of P-Type WSe2 Atomic Layers. *Nano Lett.* **2015**, *15* (1), 709−713.

(18) Chen, L.; Liu, B.; Abbas, A. N.; Ma, Y.; Fang, X.; Liu, Y.; Zhou, C. Screw-Dislocation-Driven Growth of Two-Dimensional Few-Layer and Pyramid-like WSe2 by Sulfur-Assisted Chemical Vapor Deposition. *ACS Nano* **2014**, *8* (11), 11543−11551.

(19) Eichfeld, S. M.; Hossain, L.; Lin, Y.-C.; Piasecki, A. F.; Kupp, B.; Birdwell, A. G.; Burke, R. A.; Lu, N.; Peng, X.; Li, J.; Azcatl, A.; McDonnell, S.; Wallace, R. M.; Kim, M. J.; Mayer, T. S.; Redwing, J. M.; Robinson, J. A. Highly Scalable, Atomically Thin WSe2 Grown via Metal−Organic Chemical Vapor Deposition. *ACS Nano* **2015**, *9* (2), 2080−2087.

(20) Chun, Y.-G.; Lee, W.-J.; Lee, M.; Paek, S.-M. Effect of Long-Range and Local Order of Exfoliated and Proton-Beam-Irradiated WSe2 Nanosheets for Sodium Ion Battery Application. *Bull. Korean Chem. Soc.* **2018**, *39* (5), 665−670.

(21) Chen, M.; Wang, Y.; Shepherd, N.; Huard, C.; Zhou, J.; Guo, L. J.; Lu, W.; Liang, X. Abnormal Multiple Charge Memory States in Exfoliated Few-Layer WSe2 Transistors. *ACS Nano* **2017**, *11* (1), 1091−1102.

(22) Koperski, M.; Nogajewski, K.; Arora, A.; Cherkez, V.; Mallet, P.; Veuillen, J.-Y.; Marcus, J.; Kossacki, P.; Potemski, M. Single Photon Emitters in Exfoliated WSe2 Structures. *Nat. Nanotechnol.* **2015**, *10* (6), 503−506.

(23) Hong, Y.; Kang, W.-M.; Cho, I.-T.; Shin, J.; Wu, M.; Lee, J.-H. Gas-Sensing Characteristics of Exfoliated WSe2 Field-Effect Transistors. *J. Nanosci. Nanotechnol.* **2017**, *17* (5), 3151−3154.

(24) Paul, S.; Motalab, M.; Zobayer, M. A.; Hossain, M. J. Strain Rate and Curing Condition Effects on the Stress−Strain Behaviour of Epoxy Adhesive Materials. *J. Adhes. Sci. Technol.* **2017**, *31* (16), 1782−1795.

(25) Liu, Z.; Amani, M.; Najmaei, S.; Xu, Q.; Zou, X.; Zhou, W.; Yu, T.; Qiu, C.; Birdwell, A. G.; Crowne, F. J.; Vajtai, R.; Yakobson, B. I.; Xia, Z.; Dubey, M.; Ajayan, P. M.; Lou, J. Strain and Structure Heterogeneity in MoS2 Atomic Layers Grown by Chemical Vapour Deposition. *Nat. Commun.* **2014**, *5* (1), No. 5246.

(26) Zhang, F.; Wang, Z.; Zheng, K.; Feng, C.; Yao, R.; Tao, L.; Yu, J.; Chen, X. Promoting Crystal Distribution Uniformity Based on the CVD Method with the Aid of Finite Element Methods. *Cryst. Growth Des.* **2020**, *20* (2), 777−782.

(27) Paul, S.; Momeni, K.; Levitas, V. I. Shear-Induced Diamondization of Multilayer Graphene Structures: A Computational Study. *Carbon* **2020**, *167*, 140−147.

(28) Wang, J.; Namburu, R. R.; Dubey, M.; Dongare, A. M. Origins of Ripples in CVD-Grown Few-Layered MoS2 Structures under Applied Strain at Atomic Scales. *Sci. Rep.* **2017**, *7* (1), No. 40862.

(29) Şar, H.; Özden, A.; Demiroğlu, İ.; Sevik, C.; Perkgoz, N. K.; Ay, F. Long-Term Stability Control of CVD-Grown Monolayer MoS2. *Phys. Status Solidi RRL* **2019**, *13* (7), No. 1800687.

(30) Paul, S.; Momeni, K. Mechanochemistry of Stable Diamane and Atomically Thin Diamond Films Synthesis from Bi- and Multilayer Graphene: A Computational Study. *J. Phys. Chem. C* **2019**, *123* (25), 15751−15760.

(31) Momeni, K.; Ji, Y.; Wang, Y.; Paul, S.; Neshani, S.; Yilmaz, D. E.; Shin, Y. K.; Zhang, D.; Jiang, J.-W.; Park, H. S.; Sinnott, S.; van Duin, A.; Crespi, V.; Chen, L.-Q. Multiscale Computational Understanding and Growth of 2D Materials: A Review. *npj Comput. Mater.* **2020**, *6* (1), No. 22.

(32) Briggs, N.; Subramanian, S.; Lin, Z.; Li, X.; Zhang, X.; Zhang, K.; Xiao, K.; Geohegan, D.; Wallace, R.; Chen, L.-Q.; Terrones, M.; Ebrahimi, A.; Das, S.; Redwing, J.; Hinkle, C.; Momeni, K.; van Duin, A.; Crespi, V.; Kar, S.; Robinson, J. A. A Roadmap for Electronic Grade 2D Materials. *2D Mater.* **2019**, *6* (2), No. 022001.

(33) Gao, J.; Xu, Z.; Chen, S.; Bharathi, M. S.; Zhang, Y. Computational Understanding of the Growth of 2D Materials. *Adv. Theory Simul.* **2018**, *1* (11), No. 1800085.

(34) Momeni, K.; Ji, Y.; Nayir, N.; Sakib, N.; Zhu, H.; Paul, S.; Choudhury, T. H.; Neshani, S.; Van Duin, A. C. T.; Redwing, J. M.; Chen, L.-Q. A Computational Framework for Guiding the MOCVD-Growth of Wafer-Scale 2D Materials. *npj Comput. Mater.* **2022**, *8* (1), No. 240.

(35) Momeni, K.; Attariani, H.; LeSar, R. A. Structural Transformation in Monolayer Materials: A 2D to 1D Transformation. *Phys. Chem. Chem. Phys.* **2016**, *18* (29), 19873−19879.

(36) Liu, J.; Mohan, A.; Kalia, R. K.; Nakano, A.; Nomura, K.; Vashishta, P.; Yao, K.-T. Boltzmann Machine Modeling of Layered MoS2 Synthesis on a Quantum Annealer. *Comput. Mater. Sci.* **2020**, *173*, No. 109429.

(37) Wu, J.; Hu, Z.; Jin, Z.; Lei, S.; Guo, H.; Chatterjee, K.; Zhang, J.; Yang, Y.; Li, B.; Liu, Y.; Lai, J.; Vajtai, R.; Yakobson, B.; Tang, M.; Lou, J.; Ajayan, P. M. Spiral Growth of SnSe2 Crystals by Chemical Vapor Deposition. *Adv. Mater. Interfaces* **2016**, *3* (16), No. 1600383.

(38) Ji, Y.; Momeni, K.; Chen, L.-Q. A Multiscale Insight into the Growth of H-BN: Effect of the Enclosure. *2D Mater.* **2021**, *8* (3), No. 035033.

(39) Vilá, R. A.; Momeni, K.; Wang, Q.; Bersch, B. M.; Lu, N.; Kim, M. J.; Chen, L. Q.; Robinson, J. A. Bottom-up Synthesis of Vertically Oriented Two-Dimensional Materials. *2D Mater.* **2016**, *3* (4), No. 041003.

(40) Xuan, Y.; Jain, A.; Zafar, S.; Lotfi, R.; Nayir, N.; Wang, Y.; Choudhury, T. H.; Wright, S.; Feraca, J.; Rosenbaum, L.; Redwing, J. M.; Crespi, V.; van Duin, A. C. T. Multi-Scale Modeling of Gas-Phase Reactions in Metal-Organic Chemical Vapor Deposition Growth of WSe2. *J. Cryst. Growth* **2019**, *527*, No. 125247.

(41) Srolovitz, D. J.; Dandy, D. S.; Butler, J. E.; Battaile, C. C.; Paritosh. The Integrated Multiscale Modeling of Diamond Chemical Vapor Deposition. *JOM* **1997**, *49* (9), 42−47.

(42) Zhang, F.; Momeni, K.; AlSaud, M. A.; Azizi, A.; Hainey, M. F.; Redwing, J. M.; Chen, L.-Q.; Alem, N. Controlled Synthesis of 2D Transition Metal Dichalcogenides: From Vertical to Planar MoS_2. *2D Mater.* **2017**, *4* (2), No. 025029.

(43) Rajapakse, M.; Karki, B.; Abu, U. O.; Pishgar, S.; Musa, M. R. K.; Riyadh, S. M. S.; Yu, M.; Sumanasekera, G.; Jasinski, J. B. Intercalation as a Versatile Tool for Fabrication, Property Tuning, and Phase Transitions in 2D Materials. *npj 2D Mater. Appl.* **2021**, *5* (1), No. 30.

(44) Müller, F.; Stöwe, K.; Sachdev, H. Symmetry versus Commensurability: Epitaxial Growth of Hexagonal Boron Nitride on Pt(111) From B-Trichloroborazine $(ClBNH)_3$. *Chem. Mater.* **2005**, *17* (13), 3464−3467.

(45) Li, S.; Ouyang, D.; Zhang, N.; Zhang, Y.; Murthy, A.; Li, Y.; Liu, S.; Zhai, T. Substrate Engineering for Chemical Vapor Deposition Growth of Large-Scale Two-Dimensional Transition Metal Dichalcogenides. *Adv. Mater.* **2023**, *35*, No. 2211855.

(46) Deringer, V. L.; Bernstein, N.; Bartók, A. P.; Cliffe, M. J.; Kerber, R. N.; Marbella, L. E.; Grey, C. P.; Elliott, S. R.; Csányi, G. Realistic Atomistic Structure of Amorphous Silicon from Machine-Learning-Driven Molecular Dynamics. *J. Phys. Chem. Lett.* **2018**, *9* (11), 2879−2885.

(47) Lin, Y.-C.; Jariwala, B.; Bersch, B. M.; Xu, K.; Nie, Y.; Wang, B.; Eichfeld, S. M.; Zhang, X.; Choudhury, T. H.; Pan, Y.; Addou, R.; Smyth, C. M.; Li, J.; Zhang, K.; Haque, M. A.; Fölsch, S.; Feenstra, R. M.; Wallace, R. M.; Cho, K.; Fullerton-Shirey, S. K.; Redwing, J. M.; Robinson, J. A. Realizing Large-Scale, Electronic-Grade Two-Dimensional Semiconductors. *ACS Nano* **2018**, *12* (2), 965−975.

(48) Tonndorf, P.; Schmidt, R.; Böttger, P.; Zhang, X.; Börner, J.; Liebig, A.; Albrecht, M.; Kloc, C.; Gordan, O.; Zahn, D. R. T.; De Vasconcellos, S. M.; Bratschitsch, R. Photoluminescence Emission and Raman Response of Monolayer MoS_2, MoSe_2, and WSe_2. *Opt. Express* **2013**, *21* (4), 4908−4916.

(49) Thompson, A. P.; Aktulga, H. M.; Berger, R.; Bolintineanu, D. S.; Brown, W. M.; Crozier, P. S.; in 't Veld, P. J.; Kohlmeyer, A.; Moore, S. G.; Nguyen, T. D.; Shan, R.; Stevens, M. J.; Tranchida, J.; Trott, C.; Plimpton, S. J. LAMMPS - a Flexible Simulation Tool for Particle-Based Materials Modeling at the Atomic, Meso, and Continuum Scales. *Comput. Phys. Commun.* **2022**, *271*, No. 108171.

(50) van Duin, A. C. T.; Dasgupta, S.; Lorant, F.; Goddard, W. A. ReaxFF: A Reactive Force Field for Hydrocarbons. *J. Phys. Chem. A* **2001**, *105* (41), 9396−9409.

(51) Nayir, N.; Wang, Y.; Shabnam, S.; Hickey, D. R.; Miao, L.; Zhang, X.; Bachu, S.; Alem, N.; Redwing, J.; Crespi, V. H.; van Duin, A. C. T. Modeling for Structural Engineering and Synthesis of Two-Dimensional WSe2 Using a Newly Developed ReaxFF Reactive Force Field. *J. Phys. Chem. C* **2020**, *124* (51), 28285−28297.

(52) Ostadhossein, A.; Kim, S.-Y.; Cubuk, E. D.; Qi, Y.; van Duin, A. C. T. Atomic Insight into the Lithium Storage and Diffusion Mechanism of SiO2/Al2O3 Electrodes of Lithium Ion Batteries: ReaxFF Reactive Force Field Modeling. *J. Phys. Chem. A* **2016**, *120* (13), 2114−2127.

(53) Munetoh, S.; Motooka, T.; Moriguchi, K.; Shintani, A. Interatomic Potential for Si−O Systems Using Tersoff Parameterization. *Comput. Mater. Sci.* **2007**, *39* (2), 334−339.

(54) Yuan, F.; Huang, L. Molecular Dynamics Simulation of Amorphous Silica under Uniaxial Tension: From Bulk to Nanowire. *J. Non-Cryst. Solids* **2012**, *358* (24), 3481−3487.

(55) Gutiérrez, G.; Johansson, B. Molecular Dynamics Study of Structural Properties of Amorphous Al_2O_3. *Phys. Rev. B* **2002**, *65* (10), No. 104202.

(56) Salvatore, G. A.; Münzenrieder, N.; Barraud, C.; Petti, L.; Zysset, C.; Büthe, L.; Ensslin, K.; Tröster, G. Fabrication and Transfer of Flexible Few-Layers MoS_2 Thin Film Transistors to Any Arbitrary Substrate. *ACS Nano* **2013**, *7* (10), 8809−8815.

(57) Ji, Q.; Zhang, Y.; Zhang, Y.; Liu, Z. Chemical Vapour Deposition of Group-VIB Metal Dichalcogenide Monolayers: Engineered Substrates from Amorphous to Single Crystalline. *Chem. Soc. Rev.* **2015**, *44* (9), 2587−2602.

(58) Briggs, N.; Bersch, B.; Wang, Y.; Jiang, J.; Koch, R. J.; Nayir, N.; Wang, K.; Kolmer, M.; Ko, W.; De La Fuente Duran, A.; Subramanian, S.; Dong, C.; Shallenberger, J.; Fu, M.; Zou, Q.; Chuang, Y.-W.; Gai, Z.; Li, A.-P.; Bostwick, A.; Jozwiak, C.; Chang, C.-Z.; Rotenberg, E.; Zhu, J.; Van Duin, A. C. T.; Crespi, V.; Robinson, J. A. Atomically Thin Half-van Der Waals Metals Enabled by Confinement Heteroepitaxy. *Nat. Mater.* **2020**, *19* (6), 637−643.

(59) Sakib, N.; Paul, S.; Nayir, N.; Van Duin, A. C. T.; Neshani, S.; Momeni, K. Role of Tilt Grain Boundaries on the Structural Integrity of WSe_2 Monolayers. *Phys. Chem. Chem. Phys.* **2022**, *24* (44), 27241−27249.